Research Square

Preprints are preliminary reports that have not undergone peer review.
They should not be considered conclusive, used to inform clinical practice,
or referenced by the media as validated information.

Piezoelectric manipulation and stacking-dependent magnetism in ferrovalley materials

Jia Li

lijia@cauc.edu.cn

Civil Aviation University of China

Shiyao Zhang

Civil Aviation University of China

Tong Wei

Civil Aviation University of China

Xiong Yang

Civil Aviation University of China

Limin Liu

Beihang University

Article

Keywords:

Posted Date: June 22nd, 2026

DOI: https://doi.org/10.21203/rs.3.rs-9906972/v1

License: This work is licensed under a Creative Commons Attribution 4.0 International License.
Read Full License

Additional Declarations: No competing interests reported.

Piezoelectric manipulation and stacking-dependent magnetism in ferrovalley materials

Jia Li*[,1], Shiyao Zhang[1], Tong Wei[1], Xiong Yang[1] & Limin Liu*[,2]

ABSTRACT: The electronic transport characteristics of two-dimensional (2D) systems have widespread application prospects in the fabrication of multifunctional nanodevices. However, the current research for basic transport phenomena, such as anomalous valley Hall effect (AVHE) and piezoelectric response, is limited to discrete discussion. Here, we theoretically propose a valley-piezoelectricity coupling strategy beyond the existing paradigm to realize AVHE and layer Hall effect (LHE) in ferrovalley (FV) systems, and its essential principle can be extended to general valleytronic materials. Through first-principles calculations, we demonstrate that the large polarized electric field of 2.8×10^6 (1.67×10^7) V/m can be induced by 0.1% uniaxial strain in FV 2*H*-LaHF (1*T*-LaHF) monolayers. In addition, the microscopic mechanism of interlayer antiferromagnetic (AFM) state of 2*H*-LaHF bilayer is uncovered by the spin Hamiltonian and super-superexchange (SSE) interaction. Our findings pave the way for new explorations of valley Hall-related effect involving piezoelectricity.

I. INTRODUCTION

Berry curvature, which represents the entanglement of the bands, describes the geometric properties of the wave function[1-3]. The Hall effect originates from the coupling of Berry curvature with multiple electronic degrees of freedom, including charge, spin, valley and etc[4-9].The spin degree of freedom is associated with Berry curvature in time-reversal (*T*) broken system to generate the quantum anomalous Hall

[1]College of Science, Civil Aviation University of China, Tianjin 300300, China. [2]School of Physics, Beihang University, Beijing 100191, China. e-mail: lijia@cauc.edu.cn (Jia Li); liminliu@buaa.edu.cn (Limin Liu).

effect (QAHE)[2-6], while the space-inversion (*P*) symmetry breaking in valleytronics causes valley Hall effect (VHE) to establish a connection linking unequal Berry curvature with the valley degree of freedom[10-13]. The *T*- and *P*-broken make AVHE and piezoelectric polarization often coexist in a single FV system, and the novel coupling of valley and piezoelectricity, i.e. unconventional piezoelectricity and Berry-Curvature Dopole has aroused widespread concern[14-16]. These findings suggest a rich connection between valley, Berry curvature, and piezoelectricity, however, the transport relationship between piezoelectric response and valley Hall-related effect are still lacking[10-20].

2D van der Waals (vdW) materials bring novel degree of freedom for electronic engineering due to the weak interlayer vdW interaction, and flexible vdW stacking releases highly tunable magnetic and electronic properties[20-27]. The unique layer degree of freedom and Berry curvature are interrelated to form the LHE, in which electrons in different layers experience opposite deflections due to the influence of the unequal Berry curvature[28]. The sliding ferroelectricity via interlayer sliding in YI_2 and GdI_2 bilayers[29,30], as well as the layer-polarized anomalous Hall effect (LP-AHE) caused by stacking orders in VSi_2P_4 and $MnBi_2Te_4$ bilayers[31,32], exhibits rich physical phenomena in layertronics. Therefore, it is very meaningful to explore the transport characteristics of monolayer and bilayer FV systems and the effect of stacking order on the valley behavior and intrinsic magnetism.

In this work, we propose the phenomena of novel piezoelectric anomalous valley Hall effect (PAVHE) and piezoelectric layer Hall effect (PLHE) by coupling the piezoelectric response, valley and layer degrees of freedom, which can be classified as new members of valley-related multiple Hall effect. The coexistence of large spontaneous valley polarization and tunable piezoelectric polarization makes 1*T*-LaHF and 2*H*-LaHF monolayers be ideal platforms for PAVHE. Then we take 2*H*-LaHF monolayer as an example to study the effect of bilayer stacking orders on magnetism, valley behavior and LHE. Moreover, the microscopic mechanism of interlayer magnetism is revealed by the spin Hamiltonian and interlayer electrons

hopping. This work greatly enriches the research on valley Hall-related effect, piezotronics and layertronics.

II. COMPUTATIONAL DETAILS

All structural optimization and electronic structure calculations are performed using the projector augmented wave (PAW) method through the Vienna ab initio simulation package (VASP)[33]. For exchange and correlation interactions, the generalized gradient approximation (GGA) of Perdew–Burke-Ernz-erhof functional (PBE) is treated[34]. To attain reliable results, the kinetic energy cutoff and total energy convergence criterion is set to 500 eV and 10^{-6} eV, respectively. A 20 Å vacuum layer in the z direction is used to eliminate interactions between adjacent layers. Atomic positions are fully relaxed until the maximum force on each atom is less than 0.01 eV/Å. The Monkhorst–Pack (MP) grid is chosen to be Γ-cntered 11 × 11 × 1 for electronic structure and 8×14×1 for piezoelectric stress tensors e_{ij}. The elastic stiffness and piezoelectric stress tensors (C_{ij} and e_{ij}) are calculated by using strain–stress relationship (SSR) and DFPT method. The strong correlation effects for the La-5d electrons are handled via the PBE+U scheme for the electronic structure calculations, in which a Hubbard correction U_{eff} = 5 eV is adopted and the value has credibly been used for other La-based monolayer structures[35,36]. The van der Waals interaction is included by the semiempirical DFT-D3 method[37]. The phonon dispersion is based on a 4 × 4 × 1 supercell by using the PHONOPY code[38]. Ab initio molecular dynamic (AIMD) simulations adopt the NVT ensemble based on the Nosé-Hothermostat with a total of 6.0 ps[39]. The Berry curvatures of materials is calculated using maximally localized Wannier functions implemented in the WANNIER90[40].

III. RESULTS AND DISCUSSION

A. The valley-related properties of LaHF monolayer

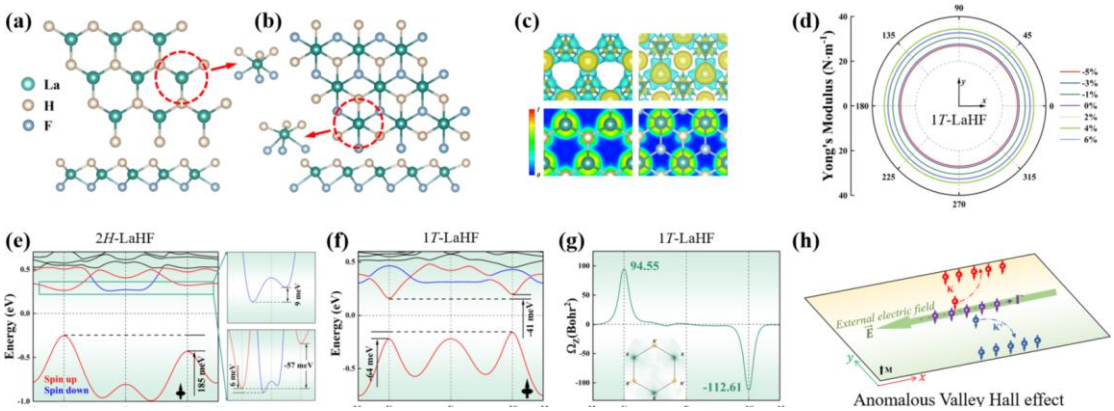


Fig. 1 Crystal structures of monolayer (a) 2*H*-LaHF and (b) 1*T*-LaHF from top and side views. The unit cell is marked by the red dashed lines. (c) The electron localization function and differential charge densities of 2*H*-LaHF and 1*T*-LaHF. (d) The Young's modulus for 1*T*-LaHF. The electronic band structures of (e) 2*H*-LaHF and (f) 1*T*-LaHF with SOC, and the black arrow indicates the magnetic moment direction of La along the z-axis. (g) The Berry curvatures of 1*T*-LaHF. (h) The diagram of AVHE with K, K' and Γ valleys carriers.

Figs. 1(a) and 1(b) exhibits the crystal structures of 2*H*-LaHF and 1*T*-LaHF with *P*-broken and a space group of *P*3*m*1 (No. 156). The in-plane lattice constant for the fully optimized species for 2*H*-LaHF and 1*T*-LaHF are 3.71 and 3.82 Å, respectively. As shown in Fig. 1(c), the electron localization function (ELF) shows that the electrons are mainly dispersed around the La, H, and F atoms, indicating their ionic bonding characteristics. To evaluate the stability of monolayer 1*T*-LaHF and 2*H*-LaHF, the phonon spectra under different biaxial strains and AIMD simulations at 300K are investigated. As shown in Fig. S1, there is not imaginary modes in the whole Brillouin Zone (BZ) , indicating the dynamic stability of 1*T*-LaHF and 2*H*-LaHF. During the AIMD simulations, the small energy fluctuations and preservation of structural integrity prove that the excellent thermal stability of 1*T*-LaHF and 2*H*-LaHF. Finally, we calculate the elastic constants $C_{11/22}$ (241.77 N/m), C_{12} (88.83 N/m) and C_{33} (8.10 N/m) of 2*H*-LaHF and $C_{11/22}$ (160.82 N/m), C_{12} (47.24 N/m) and C_{33} (9.18 N/m) of 1*T*-LaHF, respectively, which meet the Born–Huang criteria (i.e. $C_{11/22} > C_{12} > 0$, $C_{11}C_{22}$-$C_{12}^2 > 0$ and $C_{33} > 0$) [10], proving the mechanical stability of the structure. Compared with the Young's modulus of typical 2D materials such as graphene (350 N/m)[41] and 2*H*-BN (270 N/m)[42], 2*H*-LaHF and 1*T*-LaHF monolayers exhibit lower stiffness and greater flexibility (in Figs. 1(d) and S2).

In order to determine the magnetic ground states of 1*T*-LaHF and 2*H*-LaHF, the supercell of 4 × 4 × 1 was used to study the energy difference of FM, AFM-1, AFM-2 and AFM-3 (in Fig. S3), and the calculated energy difference shown in Table. S1 indicates the dominance of FM coupling in 2*H*-LaHF and 1*T*-LaHF. The physical origination of FM coupling can be explained by Goodenough-Kanamori-Anderson rules[43]. The lattice constant of 1*T*-LaHF (2*H*-LaHF) is 3.82 (3.71) Å, and the nearest-neighboring distance of La-La, La-F and La-H are 3.82 (3.71), 2.51 (2.52) and 2.34 (2.46), respectively. The large distance of La-La indicates that the direct coupling among La atoms should be weak. However, in 1*T*-LaHF (2*H*-LaHF), the angle of La-H-La and La-F-La bond are 109.65° (98.18°) and 98.85° (94.87°), respectively, which are close to 90°, implying that the indirect La-H-La and La-F-La FM super-exchange interaction leads to FM coupling in 1*T*-LaHF and 2*H*-LaHF.

With Spin-orbit-coupling (SOC) effect (in Figs. 1 and S4), based on the spin channel at the valence band maximum (VBM) and conduction band minimum (CBM), the 2H-LaHF and 1T-LaHF can be regarded as bipolar-semiconductor and half-semiconductor, respectively. It is worth noting that the large spin bandgap of 4.39 and 0.37 eV can be found in 1*T*-LaHF, which can generate 100% spin polarized carriers by electrical gating. Moreover, the valley splitting of 2*H*-LaHF and 1*T*-LaHF at CBM (VBM) is -57 (185) and -41 (-64) meV, respectively, which is larger than or comparable to those in VSe_2 (78.2 meV)[44], $LaBr_2$ (33 meV)[45] and $MoTe_2$/EuO (20 meV)[46]. The effects of biaxial strain on valley splitting, band gap, magnetic anisotropic energy (MAE) and magnetic moment are shown in Fig. S5.

The *P*-broken results in unequal nonzero Berry curvature at polarized-valleys (K and K' valleys), and the Berry curvature can be obtained from the Kubo formula[47,48]: $\Omega(k) = -\sum_n \sum_{n \neq n'} f_n \frac{2Im\langle\psi_{nk}|\hat{v}_x|\psi_{n'k}\rangle\langle\psi_{n'k}|\hat{v}_y|\psi_{nk}\rangle}{(E_n - E_{n'})^2}$ where f_n represents the Fermi-Dirac distribution. $|\psi_{nk}\rangle$ and $\hat{v}_x$ ($\hat{v}_y$) are the Bloch wave function with eigenvalue E_n and the velocity operator along x (y) direction, respectively. As shown in Figs. 1(g) and S6, the opposite signs and unequal magnitudes of polarized valleys show valley contrasting characteristics of systems. The in-plane external electric field drives the

carrier to obtain the group velocity $v_{\parallel}$, while the Berry curvature give carrier the transverse anomalous velocity $v_{\perp}$, thus producing the AVHE (in Fig. 1(h)).

B. The coupling of piezoelectric response and AVHE in FV system

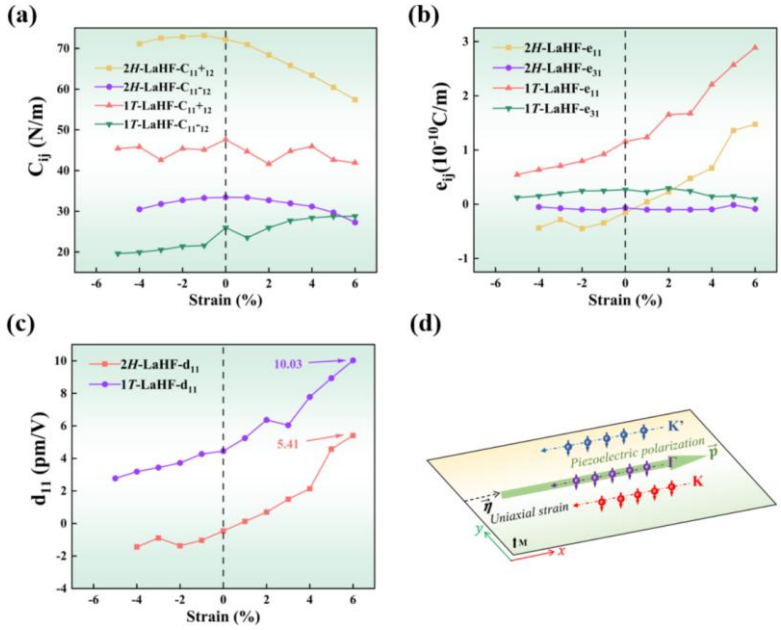


Fig. 2 (a) The elastic constants C_{jk}, (b) piezoelectric tensor e_{ij} and (c) piezoelectric strain coefficient d_{ij} as a function with biaxial strain. (d) The diagram of piezoelectric response induced by $\vec{\eta}$.

Next, we evaluated the piezoelectric property of material 2*H*-LaHF and 1*T*-LaHF. Because the Janus structure belongs to *P*3*m*1 group symmetry, using the Voigt symbol, the piezoelectric tensor e_{ik} can be expressed as:

$$e = \begin{pmatrix} e_{11} & -e_{11} & 0 \\ 0 & 0 & -e_{11} \\ e_{31} & e_{31} & 0 \end{pmatrix} . \quad (1)$$

And the piezoelectric coefficient d_{ij} can be expressed as:

$$d = \begin{pmatrix} d_{11} & -d_{11} & 0 \\ 0 & 0 & -2d_{11} \\ d_{31} & d_{31} & 0 \end{pmatrix}. \quad (2)$$

The piezoelectric coefficient d_{ik} has the following relationship with piezoelectric coefficient tensor e_{ik} and elastic coefficient C_{ik}: $e_{ik} = d_{ij}C_{jk}$. The in-plane and out-of-plane piezoelectric coefficients can be expressed as: $d_{11} = \frac{e_{11}}{C_{11}-C_{12}}$ and

$$d_{31} = \frac{e_{31}}{C_{11}+C_{12}}$$

.

In FV system, the *P*-broken results in the piezoelectric polarization as well as the unequal Berry curvature and valley polarization. A natural question is whether there is a coupled transport relationship between valley degree of freedom and piezoelectric response. The orthorhombic supercell be used to calculate the piezoelectric tensor e_{ik} of systems (see Figs. S7(a) and (b)). As shown in Fig. 2(b), the electronic and ionic contributions for piezoelectric tensor e_{ik} have opposite signs and similar values under non biaxial strain, which directly leads to the weak in-plane and out-of-plane piezoelectric response. In Figs. S7(d) and (e), with the application of tensile strain, the ionic contribution decreases rapidly while the electronic contribution is robust for piezoelectric tensor e_{11}. As shown in Fig. 2(c), the in-plane piezoelectric coefficients d_{11} of 5.41 (10.03) pm/V can be found in 2*H*-LaHF (1*T*-LaHF) under +6% biaxial strain, which is greater than most 2D Janus materials (WSTe (3.33 pm/V), SnSSe (2.25 pm/V) and MoS_2 (3.73 pm/V))[49-51]. The d_{11} of 2*H*-LaHF (1*T*-LaHF) without biaxial strain is -0.46 (4.45) pm/V, which indicates that the direction of piezoelectric polarization is opposite (same) to the direction of uniaxial strain ($\vec{\eta}$).

The use of hydrostatic pressure and nonconducting atomic force microscopy makes it possible to apply local stress to the sample. Fig. 2(d) exhibits the strain-induced piezoelectric polarization, and the related mechanism is that the polarized electric field induced by $\vec{\eta}$ excites carriers from VBM to CBM to produce the electronic output. Next, we use charge droping, which is widely used as a regulatory means, to selectively excite the carriers of the polarized-valleys. We focus on the intrinsic polarized electric field induced by $\vec{\eta}$ in piezoelectric response. The permittivity, Young's modulus and in-plane piezoelectric coefficients of 2*H*-LaHF (1*T*-LaHF) are 3.53 (4.96), 45.68 (32.68) N/m and -0.46 (4.45) pm/V, respectively. When +0.1% $\vec{\eta}$ is applied, the corresponding stress σ can be expressed as $\sigma = Y \cdot \varepsilon$, where Y and ε are Young's modulus and strain, respectively. The intrinsic polarized electric field E can be expressed as $E = \frac{d_{11} \cdot \sigma}{\varepsilon_{xx} \cdot \varepsilon_0}$, where ε_0 is permittivity of vacuum.

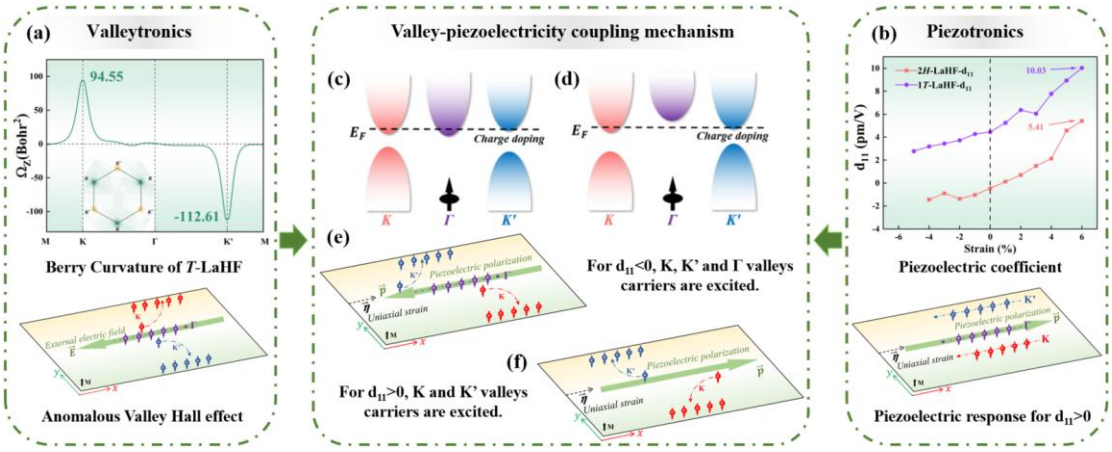


Fig. 3 The valley-piezoelectricity coupling mechanism. (a) The unequal Berry curvature and anomalous valley Hall effect. (b) The piezoelectric coefficient of LaHF monolayers and piezoelectric response. The illustration of band structure of PAVHE with Fermi energy levels penetrating polarized-valleys and Γ valley in (c) 2*H*-LaHF and polarized-valleys in (d) 1*T*-LaHF. The diagram of PAVHE in (e) 2*H*-LaHF and (f) 1*T*-LaHF. The direction of stress is opposite (same) to the direction of polarization in 2*H*-LaHF (1*T*-LaHF). The carriers from K, K' and Γ valleys are indicated using red, blue and purple markers, respectively, with arrows marking the spin orientations.

Based on the above formula, 0.1% $\vec{\eta}$ can generate an intrinsic polarized electric field of 2.8×10^6 (1.67×10^7) V/m in 2*H*-LaHF (1*T*-LaHF), which indicates the high efficiency of $\vec{\eta}$ on the induction of polarization electric field. As shown in Figs. 3(c)-(f), carrier doping can effectively regulate Fermi levels to selectively excite polarized-valleys carriers. The polarized electric field and the unequal Berry curvature cause the polarized valley carriers to obtain $v_{\parallel}$ and $v_{\perp}$, respectively. The transport phenomenon in which the intrinsic polarized electric field replaces the external electric field to drive the carrier is called PAVHE, which can be classified as one of the members of valley-related multiple Hall effect. Based on the electronic band structure, the PAVHE in 2*H*-LaHF and 1*T*-LaHF under different biaxial strain is shown in Fig. S8.

C. The stacking-dependent magnetism in 2*H*-LaHF bilayer

The stacking orders of magnetic materials bilayer may cause intriguing valley behavior and LHE. We discuss the novel physical behaviors by taking the different stacking sequences (AA-0, AA-1, AA-2, AB-0, AB-1 and AB-2) under the typical stacking of 2*H*-LaHF as an example (in Figs. 4(a)-(f)). The AA-0 stacking of 2*H*-LaHF bilayer is constructed by placing one layer facing the other layer, resulting in a

mirror symmetry and 3-fold rotation axis in xy plane. AA-1 and AA-2 stackings are constructed by interlayer translation operations of $t_{1\parallel}\left[\frac{2}{3},\frac{1}{3},0\right]$ and $t_{1\parallel}\left[\frac{1}{3},\frac{2}{3},0\right]$, respectively. AB-0 stacking can be constructed by rotating the upper layer 180° based on AA-0 stacking, while AB-1 and AB-2 stacking can be obtained from AB-0 stacking by translation operations of $t_{1\parallel}\left[\frac{2}{3},\frac{1}{3},0\right]$ and $t_{1\parallel}\left[\frac{1}{3},\frac{2}{3},0\right]$, respectively. In short, the bilayer systems conventionally constructed by Janus 2*H*-LaHF leads to the broken mirror symmetry along the z direction, which is the basis for the emergence of valley polarization and LHE[25-27].

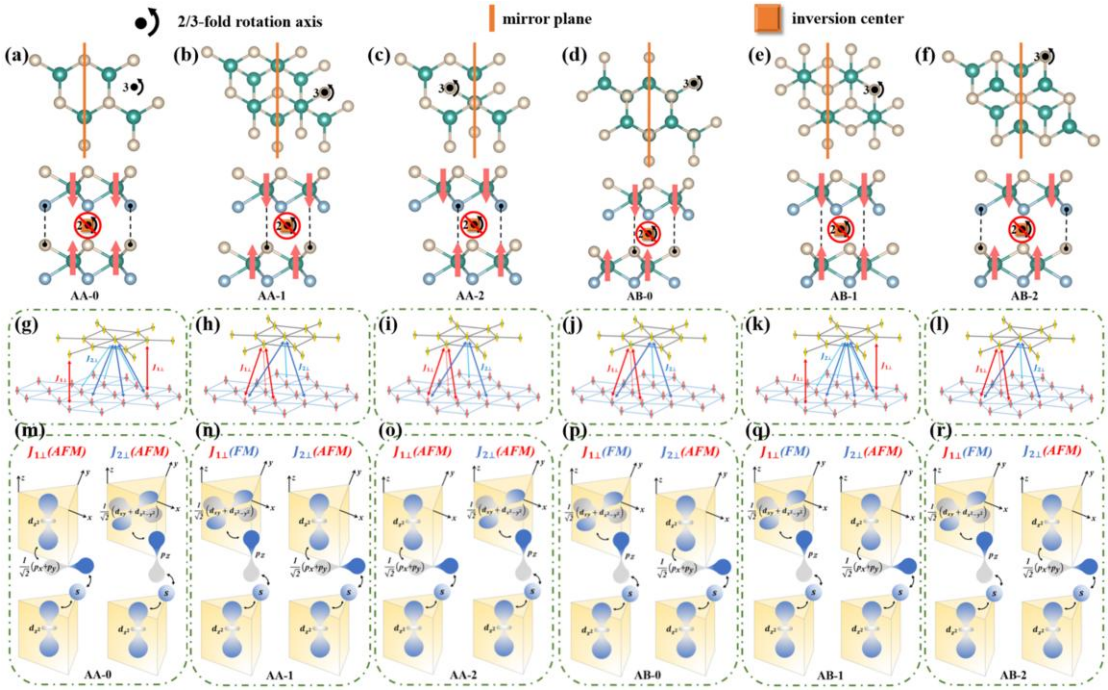


Fig. 4 (a)-(f) The stacking structures for different stacking orders, and the red arrows represent the direction of magnetization of the La atoms. (g)-(l) The interlayer La nearest neighbor and second-nearest neighbor correspond to $J_{1\perp}$ (red) and $J_{2\perp}$ (blue) for different stacking orders. (m)-(r) Schematics of SSE for different stacking orders.

As shown in Fig. S9, due to the breaking of mirror symmetry, the asymmetrical redistribution of charge density of layer-1 and layer-2 indicates the existence of out-of-plane electrical polarization. Additionally, all stacking of 2*H*-LaHF exhibit the interlayer AFM coupling (M↑↓), while AA-2 and AB-0 stacking exhibit the lowest energy, as indicated in Fig. S10(a). To understand the interlayer AFM coupling caused by stacking, a simple spin Hamiltonian is established[52]:

$$H = E_0 + \sum_{i,j} J_{\parallel} S_i \cdot S_j + \sum_{i,k} J_{1\perp} S_i \cdot S_k + \sum_{i,j} J_{2\perp} S_i \cdot S_l, \quad (3)$$

where E_0 is the ground state energy, and S_i, S_j, S_k and S_l are the magnetic moments at sites i, j, k and l, respectively. In Figs. 4(g)-(l), J is the Heisenberg exchange parameter, and $J_{\parallel}$, $J_{1\perp}$ and $J_{2\perp}$ are the intralayer, interlayer nearest-neighbor (NN) and interlayer next-nearest-neighbor (next-NN) La-La exchange interactions, respectively. The spin Hamiltonian of relevant stacking and the calculation results of relevant parameters are presented in Supporting Information and Table S2. $J_{\parallel} < 0$ indicates that the intralayer exchange is FM coupling, while the signs of $J_{1\perp}$ and $J_{2\perp}$ maybe vary with the stacking types, which reflects the change of the competition relationship between interlayer exchange interaction $J_{1\perp}$ and $J_{2\perp}$. In trigonal-prismatic crystal field, the La-*d* orbitals are split into d_{z^2}, d_{xz}/d_{yz} and $d_{xy}/d_{x^2-y^2}$ orbitals. Fig. S10(b) shows the different interlayer exchange interactions of La atoms. The d_{z^2}-d_{z^2} hopping is prohibited in FM alignment (blue), whereas it is allowed in AFM alignment (red), suggesting that the d_{z^2}-d_{z^2} hopping causes the predominantly AFM coupling[53]. Based on the local Hund coupling, the d_{z^2}-d_{xz}/d_{yz} and d_{z^2}-$d_{xy}/d_{x^2-y^2}$ hopping mainly contribute to the FM coupling[43,54]. The La-La interlayer exchange interactions are the SSE interaction mediated by H-*s* and F-*p* orbitals.

In the following, we quantitatively analyze the competitive relationship between $J_{1\perp}$ and $J_{2\perp}$ under different stackings. The interlayer La-La NN exchange interaction $J_{1\perp}$ (red) and La-La next-NN exchange interaction $J_{2\perp}$ (blue) for AA-1 stacking is shown in Fig. 4(h). Using H-*s* and F-*p* orbitals as the mediums, Fig. 4(n) shows the $J_{1\perp}$ is associated with the virtual excitations between half-filled La-d_{z^2} and empty $d_{xy}/d_{x^2-y^2}$ orbitals, which results in the interlayer FM coupling. However, $J_{2\perp}$ predominates the interlayer AFM coupling through virtual excitations between the half-filled La-d_{z^2} of layer-1 and layer-2. The AA-1 stacking contains three $J_{1\perp}$ bonds of -0.052 meV and three $J_{2\perp}$ bonds of 0.804 meV per unit cell, respectively, which means that next-NN interlayer exchange interactions dominates the AFM state for AA-1 stacking. For AB-1 stacking, the complete coincidence of the relative positions

between layer-1 and layer-2 causes the number of $J_{1\perp}$ ($J_{2\perp}$) bonds become one (six). Although the absolute value of $J_{1\perp}$ bonds (-0.475 meV) is greater than $J_{2\perp}$ bonds (0.115 meV), the number of $J_{2\perp}$ bonds is much greater than $J_{1\perp}$ bonds, which leads to the emergence of the interlayer AFM state. Although both AA-2 and AB-2 have three $J_{1\perp}$ and $J_{2\perp}$ bonds, their energy differences of FM and AFM states are quite different (see Table S2), which should be attributed to the symmetry difference (in Figs. 4(c) and (f)[30].

D. The PLHE in FV bilayer

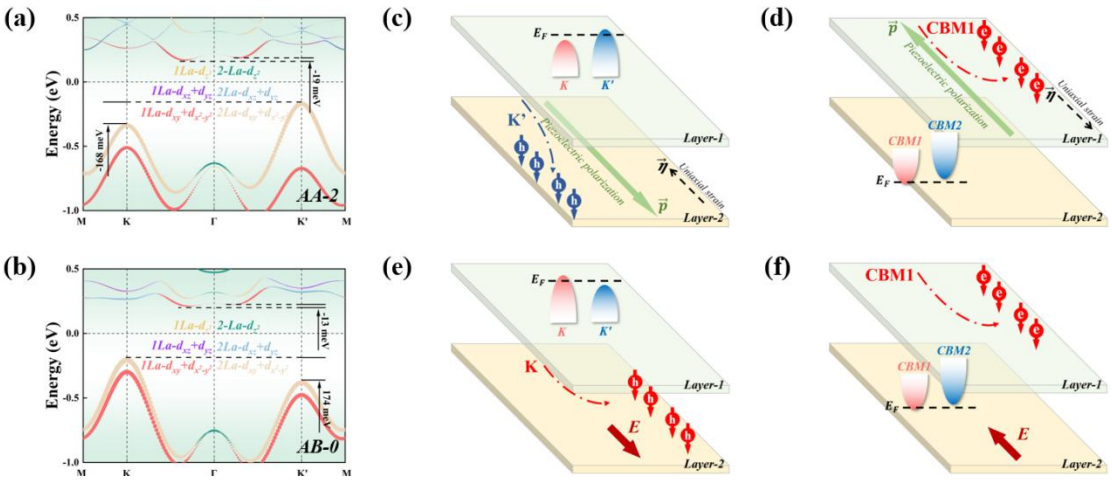


Fig. 5 The electric band structures of (a) AA-2 and (b) AB-0. Diagrams of transport phenomenon under (c) hole and (d) charge doping for AA-2 stacking. Diagrams of transport phenomenon under (e) hole and (f) charge doping for AB-0 stacking. (c), (d) and (e), (f) shows the LHE induced by the piezoelectric response and in-plane electric field, respectively. The carriers from K and K' valleys of different layers are indicated using red and blue markers, respectively, with arrows marking the spin orientations.

In the following, the electric band structures of ground-state stacking configurations (AA-2 and AB-0) are investigated based on the AFM magnetic ground state. The valley polarization can be found at VBM at K and K' points and CBM at K-Γ and K'-Γ paths (in Figs. 5(a) and (b)). Under the influence of intrinsic ferromagnetic sequence and SOC effect, VBM carriers comes from the spin-down electrons of layer-2, while CBM carriers are mainly contributed by the spin-down electrons of layer-1, indicating that AA-2 and AB-0 stacking are indirect bandgap half-semiconductors. The valley polarizations of AA-2 and AB-0 stacking at VBM

(CBM) are -168 (-19) and 174 (-13) meV under M↑↓ magnetic configuration, respectively. As shown in Fig. S11, unequal Berry curvature of AA-2 (AB-0) stacking at K and K' valleys are 16.01 (6.72) and -18.47 (-9.06) $Bohr^2$, respectively.

Considering the contribution of different layers to the polarized-valleys, different interlayer carriers can be selectively excited by carrier doping. As shown in Figs. 5(c) and (d), appropriate hole doping can excite K' valley carriers of layer-2, while the K-Γ path carriers of layer-1 can be induced by charge doping. The direction of the intrinsic polarized electric field induced by piezoelectric polarization in 2*H*-LaHF without biaxial strain is opposite to the direction of $\vec{\eta}$. In Fig. 5(c), when the inward $\vec{\eta}$ is applied to layer-2, the hole carriers move outward driven by the polarized electric field and converge to the left side of the sample under the action of Berry curvature. Charge doping excites the CBM1 valley at K-Γ path, and berry curvature and outward uniaxial strain cause charge carriers to converge on the right side of the sample. As shown in Figs. 5 and S12, with interlayer sliding, the valley polarization of VBM mostly exceeds 160 meV, while the valley of CBM transitions between K (K') and K-Γ path, suggesting 2*H*-LaHF bilayer potential applications in layertronics.

Similar to the relationship between PAVHE and AVHE, we theoretically propose the concept of PLHE involving piezoelectric response on the basis of LHE, which also can be classified as a new member of valley-related multiple Hall effect. There is no layer-related phenomenon such as sliding ferroelectricity and LP-AHE in 2*H*-LaHF bilayer[29-32], however, the existence of piezoelectric polarization and Hall effect provides a new means of regulating Bloch electrons in PAVHE and PLHE. Although we primarily focused on trigonal lattices (*P*3*m*1) to discuss PAVHE and PLHE, the principles of essentiality can also be adapted to other lattice structures, such as square lattice GaBr and GeSe monolayers (*P*4/*nmm*) and altermagnetic material CrO (*P*4/*mmm* space group)[55-57].

IV. CONCLUSION

In conclusion, we theoretically propose a novel mechanism to realize piezoelectric AVHE and LHE based on FV 2*H*-LaHF and 1*T*-LaHF monolayers. The

coexistence of unequal Berry curvature and piezoelectric response under *P*-broken makes the valley-piezoelectricity coupling mechanism is universal in 2D valleytronic materials. Based on first-principles calculations, the large intrinsic polarized electric field of 2.8×10^6 (1.67×10^7) V/m can be induced by 0.1% uniaxial strain in 2*H*-LaHF (1*T*-LaHF). Furthermore, the microscopic mechanism of interlayer AFM state in 2*H*-LaHF bilayer is revealed by spin Hamiltonian and interlayer electron hopping. Our work has great significance for the fundamental research of valley Hall-related effect, and may facilitate experimental work related to valleytronics and piezophotonics.

Data Availability

The datasets generated and/or analyzed during the current study are not publicly available due to the large aggregate size of the raw VASP output files but are available from the corresponding author on reasonable request.

Code Availability

No custom code was developed for this study. All calculations were performed using publicly available software packages (VASP, WANNIER90) cited in the Computational Details section.

Acknowledgments

This work was supported by the Natural Science Foundation of Tianjin Municipality (Grant No. 25JCLZJC00520) and Fundamental Research Funds for the Central Universities (Grant No. 3122025QD17)

Author Contributions

Shiyao Zhang and Xiong Yang performed DFT and AIMD calculations together with Tong Wei, and Jia Li and Shiyao Zhang wrote the manuscript with contributions from

Jia Li and Limin Liu supervised the project. All authors have read and approved the manuscript.

Competing interests

The authors declare no competing interests.

References

1. M. Wimmer, H. Price, I. Carusotto, and U. Peschel, Nat. Phys. **13**, 545 (2017).
2. J. Xiao, Y. Wang, H. Wang, C. D. Pemmaraju, S. Wang, P. Muscher, E. J. Sie, C. M. Nyby, T. P. Devereaux, X. Qian, X. Zhang, and A. M. Lindenberg, Nat. Phys. **16**, 1028 (2020).
3. N. Nagaosa, J. Sinova, S. Onoda, A. MacDonald, and N. Ong, Rev. Mod. Phys. **82**, 1539 (2010).
4. E. Cohen, H. Larocque, F. Bouchard, F. Nejadsattari, Y. Gefen, and E. Karimi, Nat. Rev. Phys **1**, 437 (2019).
5. Y. Deng, Y. Yu, M. Z. Shi, Z. Guo, Z. Xu, J. Wang, X. H. Chen, and Y. Zhang, Science **367**, 895 (2020).
6. Z. Liu, G. Zhao, B. Liu, Z. F. Wang, J. Yang, and F. Liu, Phys. Rev. Lett. **121**, 246401 (2018).
7. K. Mak, K. McGill, J. Park, and P. McEuen, Science **344**, 1489 (2014).
8. H. Hu, W.-Y. Tong, Y.-H. Shen, X. Wan, and C.-G. Duan, npj Comput. Mater. **6**,129 (2020).
9. D. Xiao, G.-B. Liu, W. Feng, X. Xu, and W. Yao, Phys. Rev. Lett. **108**, 196802 (2012).
10. Y. Ma, L. Kou, A. Du, B. Huang, Y. Dai, and T. Heine, Phys. Rev. B **97**, 035444 (2018).
11. T. Zhang, X. Xu, B. Huang, Y. Dai, and Y. Ma, npj Comput. Mater. **8**, 64 (2022).
12. J. Zhou, Q. Sun, and P. Jena, Phys. Rev. Lett. **119**, 046403 (2017).
13. Z. Ning, X. Ding, D.-H. Xu, and R. Wang, Phys. Rev. B **108**, 159901 (2023).
14. Y. Rouzhahong, C. Liang, J. He, X. Lin, B. Wang, and H. Li, *Nano Lett.* **24**, 1137 (2024).
15. Y. Rouzhahong, C. Liang, C. Li, B. Wang, and H. Li, *Sci. China: Phys., Mech. Astron.* **66**, 247711 (2023).
16. R.-C. Xiao, D.-F. Shao, Z.-Q. Zhang, and H. Jiang, *Phys. Rev. Appl.* **13**, 044014 (2020).
17. R. Peng, Y. Ma, X. Xu, and Z. He, *Phys. Rev. B* **102**, 035142 (2020).
18. H. Zhang, W. Yang, Y. Ning, and X. Xu, *Phys. Rev. B* **101**, 205404 (2020).
19. H.-X. Cheng, J. Zhou, W. Ji, Y.-N. Zhang, and Y.-P. Feng, *Phys. Rev. B* **103**, 125121 (2021).
20. W. Du, R. Peng, Z. He, and Y. Dai, *npj 2D Mater. Appl.* **6**, 11 (2022).
21. W. Chen, Z. Sun, Z. Wang, L. Gu, X. Xu, S. Wu, and C. Gao, *Science* **366**, 983 (2019).
22. Y. Xu, A. Ray, Y.-T. Shao, S. Jiang, K. Lee, D. Weber, J. E. Goldberger, K. Watanabe, T. Taniguchi, D. A. Muller, K. F. Mak, and J. Shan, *Nat. Nanotechnol.* **17**, 143 (2022).
23. X. Li, X. Xu, H. Zhou, H. Jia, E. Wang, H. Fu, J.-T. Sun, and S. Meng, *Nano Lett.* 2023, 23, 2839.
24. X. Xuan, Z. Zhang, C. Chen, and W. Guo, *Nano Lett.* **22**, 5379 (2022).
25. L. Li, and M. Wu, *ACS Nano* **11**, 6382 (2017).

26. K. Yasuda, X. Wang, K. Watanabe, T. Taniguchi, and P. Jarillo-Herrero, *Science* **372**, 1458 (2021).
27. S. Deb, W. Cao, N. Raab, K. Watanabe, T. Taniguchi, M. Goldstein, L. Kronik, M. Urbakh, O. Hod, and M. Ben Shalom, *Nature* **612**, 465 (2022).
28. A. Gao, Y.-F. Liu, C. Hu, J.-X. Qiu, C. Tzschaschel, B. Ghosh, S.-C. Ho, D. Bérubé, R. Chen, and H. Sun, et al. *Nature* **595**, 521 (2021).
29. Y. Wu, J. Tong, F. Luo, F. Tian, G. Qin, and X. Zhang, *Nano Lett.* **23**, 6226 (2023).
30. W. Xun, C. Wu, H. Sun, W. Zhang, Y.-Z. Wu, and P. Li, *Nano Lett.* **24**, 3541 (2024).
31. T. Zhang, X. Xu, B. Huang, Y. Dai, L. Kou, and Y. Ma, *Mater. Horiz.* **10**, 483 (2023).
32. S. Li, M. Gong, S. Cheng, H. Jiang, and X. Xie, *Natl. Sci. Rev.* **10**, 9 (2023).
33. G. Kresse, and J. Furthmüller, *Phys. Rev. B* 54, 11169 (1996).
34. J. P. Perdew, K. Burke, and M. Ernzerhof, *Phys. Rev. Lett.* 77, 3865 (1996).
35. A. I. Liechtenstein, V. I. Anisimov, and J. Zaanen, *Phys. Rev. B* 52, R5467 (1995).
36. Y. Shi, N. Jia, J. Cai, Z. Lyu, and Z. Liu, *J. Phys.: Condens. Matter* 34, 475303 (2022).
37. S. Grimme, J. Antony, S. Ehrlich, and H. Krieg, *J. Chem. Phys.* 132, 154104 (2010).
38. A. Togo, F. Oba, and I. Tanaka, *Phys. Rev. B* 78, 134106 (2008).
39. D. Bucher, L. C. T. Pierce, J. A. McCammon, and P. R. L. Markwick, *J. Chem. Theory Comput.* 7, 890 (2011).
40. N. Marzari, and D. Vanderbilt, *Phys. Rev. B* 56, 12847 (1997).
41. A. Lajevardipour, M. Neek-Amal, and F. M. Peeters, *J. Phys.: Condens. Matter.* 2012, **24**(17) 175303.
42. P. Hess, *Nanotechnology* 2017, **28** (6), 064002.
43. J. B. Goodenough, *Phys. Rev.* **100**, 564 (1955).
44. W.-Y. Tong, S.-J. Gong, X. Wan, and C.-G. Duan, *Nat. Commun.* **7**, 13612 (2016).
45. P. Zhao, Y. Ma, C. Lei, H. Wang, B. Huang, and Y. Dai, *Appl. Phys. Lett.* **115**, 261605 (2019).
46. A. Zhang, Z. Gong, Z. Zhu, A. Pan, and M. Chen, *Phys. Rev. B* **102**, 155413 (2020).
47. D. Xiao, M. C. Chang, and Q. Niu, *Rev. Mod. Phys.* **82**, 1959 (2010).
48. D. J. Thouless, M. Kohmoto, M. P. Nightingale, and M. den Nijs, *Phys. Rev. Lett*. **49**, 405 (1982).
49. L. Dong, J. Lou, and V. B. Shenoy, *ACS Nano* **11**, 8242 (2017).
50. S.-D. Guo, X.-S. Guo, R.-Y. Han, and Y. Deng, *Phys. Chem. Chem. Phys.* **21**, 24620 (2019).
51. M. N. Blonsky, H. L. Zhuang, A. K. Singh, and R. G. Hennig, *ACS Nano* **9**, 9885 (2015).
52. N. Sivadas, S. Okamoto, X. Xu, C. J. Fennie, and X. Xiao, *Nano Lett.* **18**, 7658 (2018).
53]P. W. Anderson, *Phys. Rev.* **79**, 350 (1950).
54. J. Kanamori, and *J. Phys. Chem. Solids* **10**, 87 (1959).
55. Y.-K. Zhang, J.-D. Zheng, W.-Y. Tong, Y.-F. Zhao, T.-F. Tan, Y.-H. Shen, Z. Guan, F.-Y. Yue, P.-H. Xiang, and N. Zhong, et al. *Phys. Rev. B* **108**, L241120 (2023).
56. L. C. Gomes, and A. Carvalho, *Phys. Rev. B* **92**, 085406 (2015).
57. X. Chen, D. Wang, L. Li, and B. Sanyal, *Appl. Phys. Lett.* **123**, 022402 (2023).

Supplementary Files

This is a list of supplementary files associated with this preprint. Click to download.

- SupplementaryMaterial.docx